RSC Advances

PAPER

View Article Online
View Journal | View Issue

Cite this: *RSC Adv.*, 2025, **15**, 26843

Bimetallic FeNi-MOF@Al-foam metal composites for enhanced broadband noise reduction: sound absorption performance analysis and materials structural optimization

Yang Gao, *[a] Yan Gao,[b] Xiaoxu Zhang,[b] Jingchuan Guo,[b] Guohong Tian[c] and Delika M. Weragoda[c]

Noise pollution significantly impacts human health and quality of life. This study developed FeNi-MOF@Al-FM composite materials for enhanced sound absorption and addressed limitations of traditional acoustic materials. FeNi-MOF@Al-FM composites were synthesized by loading FeNi-MOF onto aluminum foam metal (FM) substrates with various thicknesses (5–15 mm) and mass ratios (5–20%). Microscopic characterization confirmed the successful synthesis of hexagonal spindle-type FeNi-MOF structures. XRD analysis showed that nickel doping caused slight lattice changes while maintaining the crystal structure. FTIR identified characteristic functional groups, and XPS confirmed Fe–Ni co-doping with multiple nitrogen species. Acoustic testing revealed that sound absorption capacity increased with material thickness, with 15 mm composites performing best across all frequencies. At a fixed 5 mm thickness, increased FeNi-MOF loading significantly enhanced absorption, as 20% mass ratio composites achieved an absorption coefficient of 0.82 at 4000 Hz, representing a 3.7-fold improvement over unloaded samples. Absorption mechanisms were proposed: low-frequency resonance absorption (600 Hz) originating from microstructures between MOF and foam metal, and high-frequency porous absorption resulting from viscous/thermal dissipation within hierarchical pores. These findings establish structure–performance relationships for FeNi-MOF@Al-FM composites and demonstrate potential applications in noise control, architectural acoustics, and instrument vibration isolation.

Received 11th May 2025
Accepted 22nd July 2025

DOI: 10.1039/d5ra03316k

rsc.li/rsc-advances

1. Introduction

Noise pollution, as one of the four major environmental pollutants of the contemporary era, has become a significant issue affecting human quality of life and health.[1,2] According to World Health Organization (WHO) studies, prolonged noise exposure induces not only auditory system deterioration but also systemic health risks, including hypertension, cardiovascular disorders, attention deficits, and broader psychophysiological impairments.[3] With the acceleration of global industrialization and urbanization, noise pollution from human activities such as transportation, construction, and industrial production has become increasingly prevalent and intense, with its negative impacts becoming more pronounced.[4] Therefore, developing efficient and innovative sound-absorbing materials has become an urgent need in the field of noise control.

Traditional sound-absorbing materials such as porous foams and mineral wool play important roles in noise control, but they still have performance limitations in specific application scenarios, such as narrow frequency response ranges, poor material stability, and insufficient environmental adaptability.[5,6] Particularly in high-frequency noise control, complex acoustic environments, and special working conditions, the sound absorption effects of these materials often cannot meet practical requirements. Therefore, the creation of high-efficiency sound-absorbing materials represents a paradigm-shifting endeavor, combining fundamental research significance in material science with multifunctional potential for real-world noise abatement applications.[7,8] Porous materials, distinguished by their inherent structural advantages including tunable porosity, extensive surface area, enhanced flexibility, and superior manufacturability, represent a dominant research paradigm in sound-absorbing material development.[9] These systems are typically classified by their microstructural configurations into three principal categories: honeycomb, fibrous, and particulate. When sound waves propagate through porous

[a]School of Music, Qilu Normal University, Jinan, 250200, China. E-mail: 20156378@qlnu.edu.cn
[b]School of Thermal Engineering, Shandong Jianzhu University, Jinan, 250013, China
[c]School of Mechanical Engineering Sciences, University of Surrey, Guildford, Surrey, GU2 7XH, UK

materials, energy dissipation occurs through the complex pore structure inside the material, mainly including viscous loss, thermal loss, and structural resonance mechanisms.

To optimize the sound absorption performance of porous materials, researchers have conducted extensive functional modification studies. Surface modification, as an important material functionalization method, can impart new functional characteristics to porous matrices while maintaining the basic properties of the materials. Recent advancements in porous composite engineering have yielded novel architectures including polyethylene-reinforced flexible polyurethane matrices, lignocellulosic-PU hybrids through chemical functionalization, carbon nanotube-embedded PU nanocomposites, and graphene oxide-integrated melamine foam systems.[10,11] These studies have made significant progress in the field of acoustic materials.

The more fibers there are inside a porous material and the finer the fibers are, the more tortuous the path of sound wave propagation will be, which can enhance the sound absorption effect. Honeycomb and fiber materials represented by melamine foam and polyvinyl alcohol (PVA) are composed of fine filament network structures and are mainly used for sound absorption and heat insulation.[12] However, existing porous sound-absorbing materials still have some defects, such as brittleness issues, complex preparation processes, and thickness limitations, resulting in unsatisfactory sound absorption performance in specific frequency ranges.[13,14] Therefore, developing new composite sound-absorbing materials to overcome these shortcomings has become a focus of current research.

Among various sound-absorbing materials, bimetallic sound-absorbing materials have attracted extensive attention from researchers due to their structural diversity, excellent mechanical properties, and good corrosion resistance.[15,16] Typically fabricated through processes such as explosive welding, roll bonding, or powder metallurgy, bimetallic sound-absorbing materials combine the physical and mechanical advantages of two distinct metals. For instance, in nickel-iron alloy materials, adjusting the compression ratio can significantly enhance the average sound absorption coefficient from 56.89% to 88.97%, demonstrating remarkable improvement.[17] Furthermore, the surface of bimetallic materials can be modified with microcellular foaming, perforations, or honeycomb structural designs to further promote multiple scattering and dissipation of sound waves, thereby achieving superior sound absorption performance.[18,19]

From the perspective of sound absorption mechanisms, the multilayer interfaces and porous structures of bimetallic materials facilitate the conversion of acoustic energy into thermal energy, reducing sound wave reflection. Additionally, the high thermal conductivity of metals accelerates the conduction and diffusion of acoustic energy into heat, improving overall sound absorption efficiency.[20–22] In recent years, researchers have systematically investigated the acoustic performance of bimetallic sound-absorbing materials across different frequency ranges and structural parameters using finite element simulations, experimental measurements, and multiscale modeling. These efforts have led to significant advancements in applications such as traffic noise control, industrial equipment noise reduction, and architectural acoustics.[23–25]

Metal–Organic Frameworks (MOF), a novel class of crystalline hybrid materials, are synthesized through coordination-driven assembly of metal nodes (ions/clusters) and organic bridging ligands.[26] These structures are characterized by precisely engineered porosity, exceptional surface-area-to-volume ratios, and programmable pore geometries, enabling transformative applications in molecular separation, heterogeneous catalysis, and advanced sensing technologies.[27] Among these, Fe-MOF derivatives demonstrate superior thermochemical resilience, stemming from robust metal–ligand coordination networks and the redox-active nature of iron centers.[28]

Recent research suggests that the unique structural characteristics of MOF materials have potential advantages in sound wave absorption.[29] MOF materials can be viewed as acoustic metamaterials capable of abnormally absorbing sound energy. Compared with traditional sound-absorbing materials, MOF materials have the following advantages:[30,31] their highly ordered pore structures provide ideal channels for sound wave propagation; their ultra-high specific surface area can significantly increase the contact area between sound waves and materials, enhancing viscous loss; the framework structure of MOF materials can resonate with sound waves, further enhancing sound energy dissipation; by regulating the pore size, porosity, and framework structure of MOF materials, selective absorption of sound waves at different frequencies can be achieved.

During the propagation of sound waves, energy loss is mainly realized through mechanisms such as viscous loss, thermal loss, and structural resonance.[32] The porous structure of MOF materials provides an ideal environment for these energy dissipation mechanisms: complex pore structures promote multiple scattering of sound waves; large specific surface area enhances the interaction between sound waves and material interfaces; adjustable pore size distribution enables materials to respond to sound waves of different frequencies.[33] These characteristics give MOF materials enormous potential in acoustic applications.[34]

Although MOF materials have demonstrated excellent performance in multiple fields, the application research of them in noise control is still in its infancy. Especially, the research on the acoustic application of iron–nickel-based MOF-derived hybrid materials is still insufficient. Addressing this research gap, this paper proposes a composite material based on foam metal (FM) supporting iron–nickel MOF. Typical MIL-88 is selected as the representative material of MOF, and aluminum foam metal is used as the supporting substrate, aiming to develop a new type of acoustic material with efficient sound absorption performance.

2. Research methods

2.1. Preparation of FeNi-MOF and FeNi-MOF@Al-FM

All chemicals employed in this investigation were analytical-grade reagents and were utilized as received without

additional purification. The following materials were used for synthesis and characterization: nickel(II) nitrate hexahydrate ($Ni(NO_3)_2 \cdot 6H_2O$, ≥99.5%, Macklin Biochemical Co., Ltd., Shanghai, China), iron(III) chloride hexahydrate ($FeCl_3 \cdot 6H_2O$, ≥99.5%, Macklin), 2-methylimidazole ($C_4H_6N_2$, ≥99.5%, Macklin), methanol (CH_3OH, ≥99%, Sinopharm Chemical Reagent Co., Ltd., Beijing, China), and deionized water (resistivity >18 MΩ cm) produced in-house using a Milli-Q water purification system. The aluminum foam metal (Al-FM) was sourced from Beifeng Metal Products Co., Ltd.

2.1.1. Preparation of FeNi-MOF. Based on optimized results from preliminary preparation experiments and accumulated experimental experience within the research group,[27–30] this study adopted a modified solvothermal method to synthesize FeNi-MOF materials. The synthesis procedure was performed as follows: precise quantities of precursors were measured using an analytical balance (0.500 g of 2-aminoterephthalic acid (NH_2-BDC), 0.380 g $FeCl_3 \cdot 6H_2O$, and 0.400 g $Ni(NO_3)_2 \cdot 6H_2O$). The measured precursors were subsequently dissolved in 50.0 mL of anhydrous *N*,*N*-dimethylformamide (DMF, 99.8% purity). The mixture was subjected to magnetic stirring (600 rpm) at room temperature (25 ± 1 °C) until complete dissolution was achieved (typically within 30 minutes).

The resulting solution was placed in an XHMC-1 microwave synthesis reactor and subjected to microwave irradiation treatment at 75 °C with 900 W power for 20 min. Subsequently, the mixture was continuously stirred under magnetic conditions with a surface magnetic flux density of 3200–3400 G and magnetic gravitational force of 10.78 N for 2 h to ensure thorough and uniform reaction.

The reaction mixture was transferred to a 100 mL Teflon-lined stainless steel autoclave and subjected to solvothermal treatment at 120 °C for 24 h in a forced convection oven. Following natural cooling to ambient temperature (25 ± 2 °C), the resulting suspension was centrifuged (4000 rpm, 10 min) using a benchtop centrifuge to isolate the brown particulate product. Purification involved sequential washing cycles: three washes with *N*,*N*-dimethylformamide (50 mL each) to remove organic residues; three washes with absolute ethanol (50 mL each) to eliminate solvent impurities; each wash cycle included 10 min of ultrasonication (40 kHz) followed by centrifugation. The purified product was subsequently dried in an oven at 80 °C for 12 h. The dried product was then ground and sieved to obtain FeNi-MOF powder with particle sizes between 20-50 mesh.

2.1.2. Preparation of FeNi-MOF@Al-FM composites. A series of FeNi-MOF@Al-FM composites were prepared using an impregnation method. First, the original Al-FM was cut into circular samples with a diameter of 100 mm or 29 mm, with the thicknesses of 5 mm, 10 mm, and 15 mm, respectively. The 100 mm diameter samples were employed for acoustic testing in the 100–1000 Hz frequency range, while the 29 mm diameter samples were utilized for measurements in the 1000–4000 Hz band. To remove surface impurities, the samples were sequentially cleaned three times with 0.1 mol L^{-1} nitric acid solution and 75% (v/v) ethanol solution (300 mL) to ensure complete removal of surface contaminants and oil residues.

In the acoustic experiments with different thickness composites, the mass of 5 mm thick Al-FM was used as the mass reference value. FeNi-MOF powder equivalent to 5% of the reference mass was weighed and dispersed in ethanol solution, followed by ultrasonic dispersion for 20 min to obtain a homogeneous suspension. The pretreated aluminum foam samples (with thicknesses of 5 mm, 10 mm, and 15 mm) were then separately immersed in three identical suspensions and slowly rotated for 20 min to ensure complete penetration of the suspension into the porous structure of Al-FM without any residual air bubbles. The prepared samples were dried at 70 °C with forced air circulation for 24 h, ultimately yielding FeNi-MOF@Al-FM-*x* composites of different thicknesses, where *x* represents the thickness value of Al-FM.

For the acoustic experiments with different loading amounts, the mass of 5 mm thick Al-FM was again used as the mass reference value. FeNi-MOF powder equivalent to 5%, 10%, and 20% of the reference mass was weighed and used to prepare separate suspensions. Three identical 5 mm thick Al-FM samples were then immersed in these suspensions following the same procedure described above, ultimately yielding *y*FeNi-MOF@Al-FM-5 composites with different loading amounts, where *y* represents the mass percentage of FeNi-MOF.

2.2. Material characterization methods

The surface microstructures of FeNi-MOF and FeNi-MOF@Al-FM composites were analyzed using a Sigma 300 field emission scanning electron microscope (SEM) with a maximum resolution of 1 nm and an adjustable acceleration voltage range of 0.1–30 kV. Prior to imaging, all samples were sputter-coated with gold to enhance conductivity and ensure clear visualization.

Crystalline phase identification and crystallinity evaluation were performed *via* X-ray diffraction (XRD) on a Rigaku Smart Lab SE X-ray diffractometer equipped with Cu target Kα radiation ($\lambda = 1.5418$ Å). Measurements were conducted at 40 mA and 40 kV, with scanning angles (2θ) spanning 5–90° or 5–50°, a scan rate of 10° min^{-1}, and a step size of 0.02°. Acquired diffraction patterns were cross-referenced with the International Centre for Diffraction Data (ICDD) database to assess phase composition and structural features.

Functional groups and chemical bonding characteristics were investigated using a Tensor 27 Fourier-transform infrared (FTIR) spectrometer. Spectra were collected across a wavenumber range of 500–4000 cm^{-1} at a resolution of 4 cm^{-1} to elucidate molecular structural details.

Thermal stability and decomposition behavior were evaluated *via* thermogravimetric analysis (TGA) on a TGA/DSC 3+ simultaneous thermal analyzer. Experiments were conducted under a nitrogen atmosphere (50 mL min^{-1} flow rate) with a temperature ramp from 25 °C to 800 °C at 5 °C min^{-1}, enabling the determination of mass-loss profiles, thermal degradation patterns, and residue composition.

Surface elemental distribution and chemical states were probed by X-ray photoelectron spectroscopy (XPS) using an

Escalab 250 Xi system with Al Kα excitation (1486.6 eV). All spectra were energy-calibrated against the C 1s peak (284.0 eV) to ensure data accuracy. Elemental oxidation states and chemical environments were deduced through deconvolution of peak positions, intensities, and line shapes in high-resolution spectra.

2.3. Acoustic performance measurement methods

This study used a standard test device to characterize the acoustic performance of materials, which mainly consists of a hollow cylindrical sound impedance tube with two microphone ports, as shown in Fig. 1. The experimental setup consisted of an impedance tube with a test sample holder mounted at one end and a sound source positioned at the opposite end.

To cover the frequency range of 100 Hz to 4000 Hz, two impedance tubes with different inner diameters were employed in this study. A 100 mm diameter impedance tube, with a measurement range of 50 Hz to 1.6 kHz, was used for the 100 Hz to 1000 Hz frequency band. This tube accommodated FeNi-MOF@Al-FM composite samples measuring 100 mm in diameter. For the higher frequency range of 1000 Hz to 4000 Hz, a 29 mm diameter impedance tube with a measurement range of 500 Hz to 6.4 kHz was utilized, testing 29 mm diameter composite samples.

The test samples completely filled the tube cross-sections, with high-viscosity sealant (modeling clay) applied around the edges to prevent any lateral sound leakage. All samples maintained uniform thickness and smooth surfaces to minimize high-frequency (*e.g.*, 4000 Hz) wave scattering caused by surface irregularities, which could interfere with standing wave formation in the tube. During installation, special care was taken to ensure the samples remained perpendicular to the tube walls without excessive compression that might alter thickness or deform internal structures. The entire preparation process preserved the samples' physical properties (density, porosity, *etc.*) to match their actual application conditions.

All measurements were performed under controlled environmental parameters, maintaining a temperature of 23 ± 1.5 °C and relative humidity of 50 ± 20%. A B&K 4231 acoustic calibrator was employed to verify system accuracy prior to testing. The normal incidence sound absorption coefficient of the materials was rigorously evaluated in compliance with the ASTM E1050-98 standard, utilizing the two-microphone impedance tube methodology to ensure precise characterization of acoustic performance. During the testing process, broadband signals emitted by the noise source produced plane sound waves in the tube, and data acquisition and processing were performed through a high-precision digital frequency analysis system. The normal incidence acoustic characteristic parameters of the samples were determined through precise analysis of the experimental transfer function.

To ensure measurement reliability and accuracy, each sample underwent triplicate testing. The results demonstrated excellent repeatability in sound absorption performance, with standard deviations remaining below 0.1 across the entire frequency spectrum. Given this high consistency, error bars were intentionally omitted from subsequent graphical representations of sound absorption data to streamline data visualization and enhance interpretability.

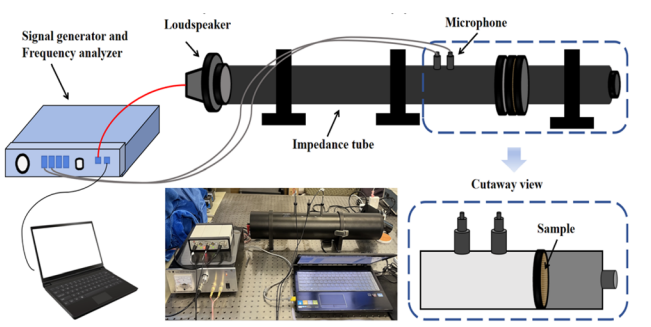

Fig. 1 Schematic diagram and physical image of impedance tube system for testing sound absorption performance of materials.

2.4. Calculation method of sound absorption coefficient

The sound absorption coefficient of a material can be determined using impedance tube testing, with two primary calculation methods: the standing wave ratio method and the transfer function method.[35,36] The standing wave ratio method has the advantage of relatively simple measurement principles but suffers from cumbersome operations when measuring sound absorption coefficients at multiple frequency points. In contrast, the transfer function method offers greater convenience by allowing simultaneous measurement of all parameters across the desired frequency range. Additionally, through mathematical modeling and signal processing, this method enables high-precision system characteristic analysis, making it suitable for more complex systems and applications.[37] Therefore, this study employs the transfer function method for calculating the sound absorption coefficient.

The transfer function, based on Laplace transform theory, establishes a relationship between the input and output quantities of a linear time-invariant system by describing its intrinsic parameters.[38] Even when the internal structure of the system is unclear or entirely unknown, the system's functionality and inherent characteristics can still be investigated by analyzing its output in response to a given input. The ASTM E1050-98 standard defines the procedure for measuring sound absorption coefficients and acoustic impedance using the transfer function method in an impedance tube, providing a consistent and accurate approach for determining the sound absorption properties of materials.

The incident sound pressure P_I and the reflected sound pressure P_R can be expressed as:

$$P_I = P_i e^{jk_0 x} \quad (1)$$

$$P_R = P_r e^{-jk_0 x} \quad (2)$$

$$k_0 = k_0' - jk_0'' \quad (3)$$

where P_i is the amplitude of P_I at the reference plane $(x = 0)$, P_r is the amplitude of P_R at the reference plane $(x = 0)$, k_0 is the complex wavenumber.

If two microphones are positioned at distances x_1 and x_2 from the material, the sound pressures P_1 and P_2 at these locations can be written as

$$P_1 = P_i e^{jk_0x_1} + P_r e^{-jk_0x_1} \quad (4)$$

$$P_2 = P_i e^{jk_0x_2} + P_r e^{-jk_0x_2} \quad (5)$$

The transfer function of the incident wave H_I is

$$H_I = \frac{P_{1I}}{P_{2I}} = e^{jk_0(x_1-x_2)} \quad (6)$$

The transfer function of the reflected wave H_R is

$$H_R = \frac{P_{1R}}{P_{2R}} = e^{-jk_0(x_1-x_2)} \quad (7)$$

Since $P_r = rP_i$, where r is the normal reflection coefficient, the transfer function of the total sound field H_{12} is

$$H_{12} = \frac{P_2}{P_1} = \frac{e^{jk_0x_2} + r\,e^{-jk_0x_2}}{e^{jk_0x_1} + r\,e^{-jk_0x_1}} \quad (8)$$

From the expressions of H_{12}, H_R and H_I, the reflection coefficient r can be derived as

$$r = \frac{H_{12} - H_I}{H_R - H_{12}}\, e^{2jk_0x_1} \quad (9)$$

By determining the variables H_{12}, x_1 and k_0 in the equation, the sound reflection coefficient r can be obtained. According to the definition of the sound absorption coefficient, the normal incidence sound absorption coefficient α is the ratio of the sound power entering the specimen surface to the incident sound power for a normally incident plane wave. The normal reflection coefficient r is the complex ratio of the reflected wave amplitude to the incident wave amplitude at the reference plane. Thus, the expression for the normal incidence sound absorption coefficient is

$$\alpha = 1 - |r|^2 \quad (10)$$

3. Results and discussion

3.1. Physicochemical analysis

3.1.1. Scanning electron microscopy (SEM) analysis. As shown in Fig. 2(a) and (b), after loading with FeNi-MOF, the color of Al-FM discs changed significantly, transforming from cyan-gray to yellowish-brown. Direct observation clearly shows powder-like particles attached to the Al-FM surface. Fig. 2(c)–(e) sequentially displays the attachment of FeNi-MOF in the Al-FM channels at mass ratios of 5%, 10%, and 20%. With the increasing proportion of FeNi-MOF attachment, particles on the Al-FM framework noticeably increased, generally attaching relatively uniformly to the channel walls and porous framework without blocking the channels of the foam metal.

During the process of increasing FeNi-MOF loading, the open pores inside the Al-FM became surrounded, forming semi-open pore structures. Considering the processing performance and microstructure of this type of composite material, further increasing the FeNi-MOF loading could have produced adverse effects. For example, excessive loading risked blocking the interconnected channel structures inside the Al-FM framework, potentially creating blind holes and closed channel structures that might have reduced sound damping effectiveness.

High-resolution SEM imaging revealed the microstructural characteristics of synthesized FeNi-MOF particles. Fig. 2(g) and (h) demonstrated that the material adopted hexagonal spindle-like crystallites with uniform surfaces, morphologically analogous to the prototypical MIL-88(Fe) framework. Despite retaining the hexagonal spindle morphology, limited nickel doping concentrations induced localized structural imperfections, manifesting as reduced crystallite dimensions within the spindles. This phenomenon was potentially attributable to the partial formation of Ni-NH_2-BDC complexes within the matrix. Complementary XRD analysis corroborated these observations, indicating either suppressed crystallographic ordering or sub-resolution crystallite sizes below detection thresholds.[39]

3.1.2. X-ray diffraction (XRD) analysis. In Fig. 3, the XRD patterns of FeNi-MOF and simulated MIL-88(Fe) were exhibited. Through comparative analysis, distinct crystalline structural characteristics were clearly observed in the prepared FeNi-MOF sample. The X-ray diffraction profile of FeNi-MOF exhibited prominent peaks at 2θ = 9.26°, 10.43°, 13.15°, 16.74°, and 20.96°, demonstrating strong alignment with the simulated MIL-88(Fe) reference pattern. These reflections corresponded to the (002), (101), (102), (103), and (202) crystallographic planes, respectively, confirming structural congruence with the MIL-88(Fe) framework as documented in prior studies.[40]

Compared with the computer-simulated MIL-88(Fe), the experimentally synthesized FeNi-MOF showed a small angular shift of about 0.14° in the diffraction peak near 9.16°. This shift phenomenon indicated that the doping of nickel elements led to minor changes in lattice parameters, thereby affecting the interplanar spacing. Additionally, the introduction of nickel elements resulted in significantly enhanced diffraction peak intensities at 13.07° and 16.64° for FeNi-MOF, further confirming that nickel elements had been successfully incorporated into the MOF framework structure and exerted certain effects on its crystalline structure.

XRD analysis verified the structural matching degree between FeNi-MOF and MIL-88(Fe) prototypes, and clarified the modulation ability of Ni incorporation on crystallographic parameters. The good correspondence of characteristic diffraction peaks suggested that despite the introduction of nickel elements, FeNi-MOF maintained the basic crystal structure of MIL-88(Fe), with only minor changes occurring in specific crystal plane directions. These findings provided important evidence for subsequent research on the structure–property relationship of bimetallic MOF materials.

3.1.3. Fourier transform infrared spectroscopy (FTIR) analysis. The FTIR spectrum of FeNi-MOF shown in Fig. 4

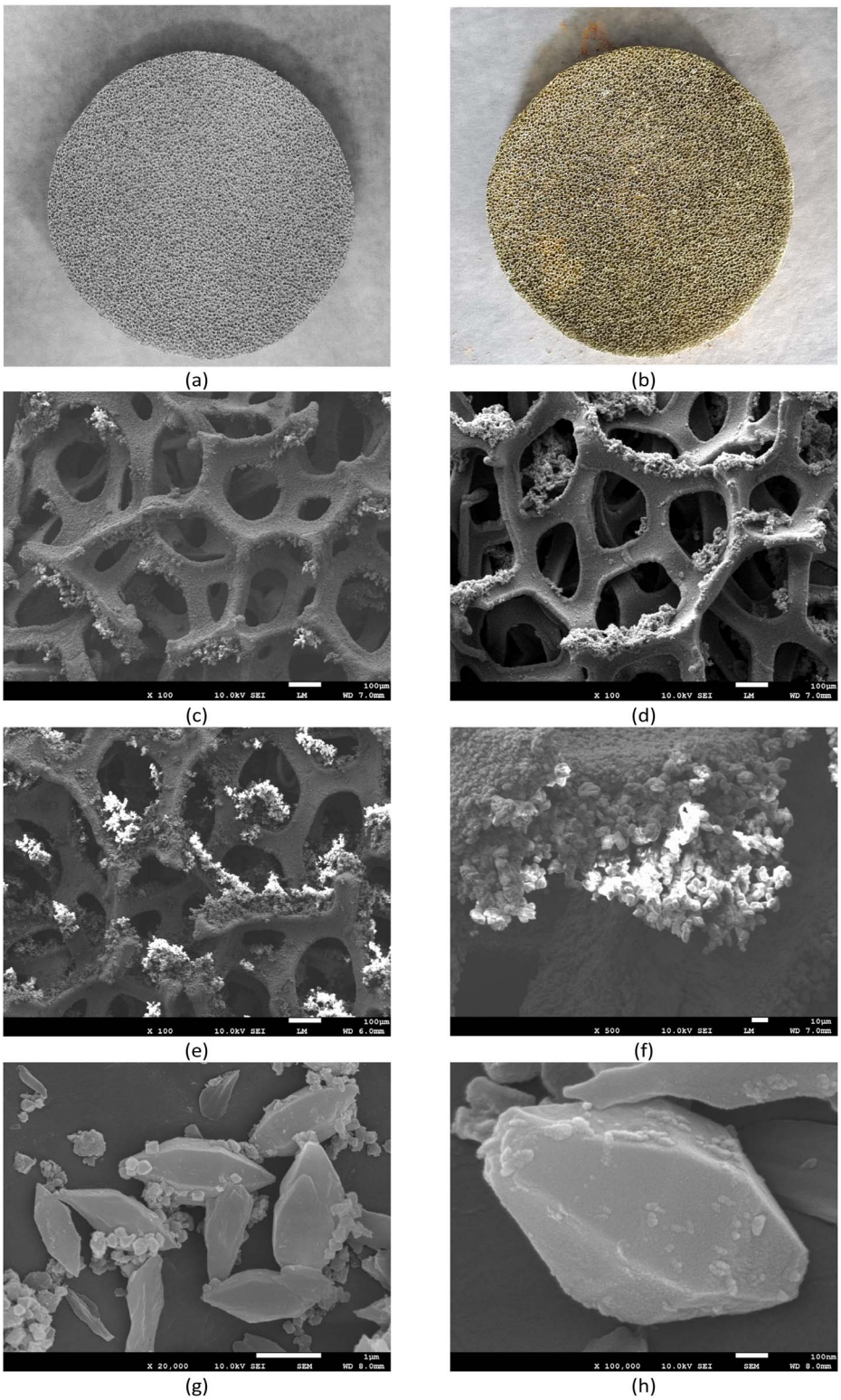

Fig. 2 Macroscopic images of Al-FM samples and SEM images of FeNi-MOF@Al-FM: (a) macroscopic image of Al-FM material without FeNi-MOF loading; (b) macroscopic image of Al-FM material loaded with FeNi-MOF; (c) SEM of Al-FM with FeNi-MOF loading ratio of 5%; (d) SEM of Al-FM with FeNi-MOF loading ratio of 10%; (e) SEM of Al-FM with FeNi-MOF loading ratio of 20%; (f) SEM of FeNi-MOF particles on Al-FM; (g) SEM of FeNi-MOF crystallites; (h) SEM of a single FeNi-MOF crystallite.

provided critical insights into its molecular composition through characteristic vibrational signatures. Detailed analysis of these spectral features revealed excellent agreement with reference MIL-88(Fe) patterns, thereby independently verifying the crystalline framework structure initially identified by XRD characterization.

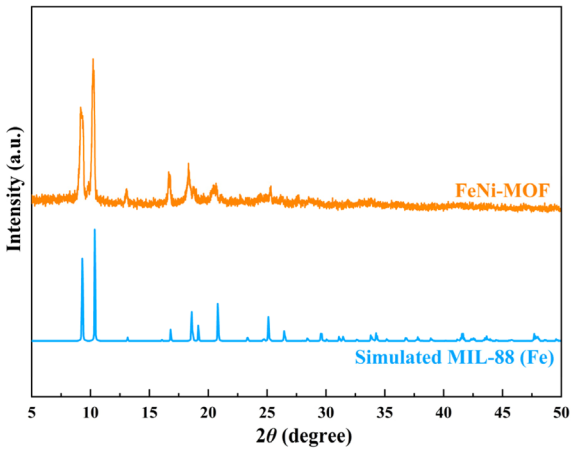

Fig. 3 XRD pattern of FeNi-MOF.

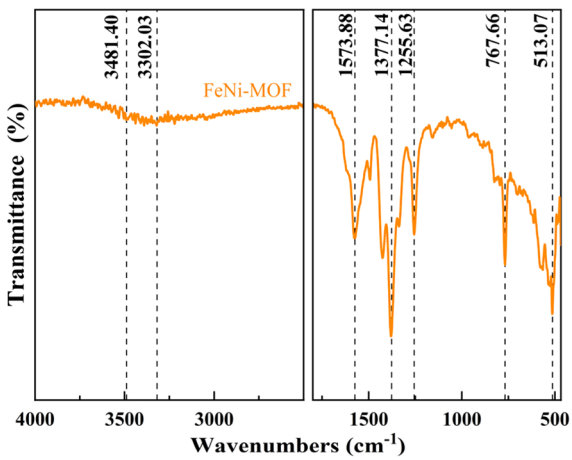

Fig. 4 FTIR curves of FeNi-MOF.

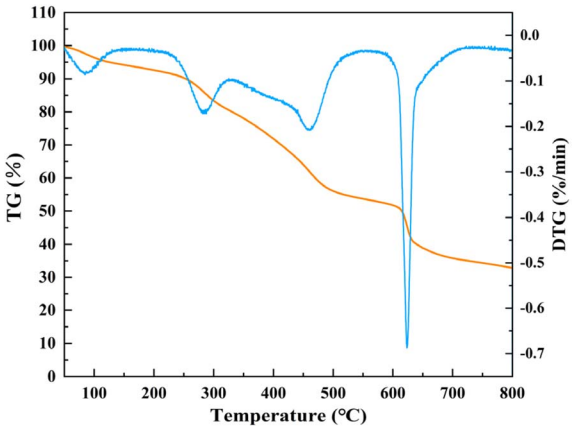

Fig. 5 TGA test results of FeNi-MOF.

In the high-frequency range (3000–3500 cm^{-1}), two prominent bands at 3481.40 cm^{-1} and 3303 cm^{-1} arose from N–H stretching modes, confirming the incorporation of amino functionalities. The mid-frequency region displayed characteristic carboxylate vibrations, with bands at 1573.88 cm^{-1} (asymmetric COO^- stretch) and 1377.14 cm^{-1} (symmetric COO^- stretch),[41] verifying the presence of carboxylate groups in the organic linkers. Additional spectral features included: a C–N stretching vibration at 1255.63 cm^{-1}; aromatic C–H out-of-plane deformation at 765.66 cm^{-1}; and a metal–oxygen coordination band at 513.07 cm^{-1} (Fe–O vibration), which provided direct evidence of coordination bond formation between the organic framework and metal centers.

The clear identification and attribution of various characteristic functional groups in the FTIR spectrum provided strong spectroscopic evidence for the successful synthesis of FeNi-MOF, which mutually corroborated with the XRD results, jointly confirming the successful preparation of the target material.

3.1.4. Thermogravimetric analysis (TGA). The thermal decomposition behavior of FeNi-MOF was systematically examined by TGA, as presented in Fig. 5. The obtained thermogram and its derivative (DTG) profile demonstrated a stepwise degradation mechanism occurring between 25-800 °C. The first mass loss event ($\Delta m \approx 5\%$), observed below 100 °C, originated from the liberation of physisorbed water and trapped solvent molecules within the porous architecture. Subsequent thermal treatment (100–300 °C) induced framework modification through progressive elimination of surface-bound functional moieties, accounting for an additional 5–10% mass reduction.

The most significant weight loss (approximately 30%) occurred in the third stage (300–500 °C), where the DTG curve showed a broad peak around 400 °C. This substantial mass reduction implied the collapse of the FeNi-MOF framework as organic ligands decomposed, leading to structural deterioration. Between 500–600 °C, a more moderate weight loss was observed, indicating the formation of nitrogen-doped carbon materials and partial reduction of metal salts to their elemental states. A sharp DTG peak appeared around 600 °C, corresponding to a rapid weight loss process, after which the TG curve gradually stabilized.

This final decomposition step represented the complete carbonization of remaining organic components and the formation of stable metal/carbon composites. By 800 °C, the weight loss had reached a plateau at approximately 35% of the original mass, indicating complete transformation into thermally stable products.

3.1.5. X-ray photoelectron spectroscopy (XPS). To gain comprehensive insights into the surface chemistry of FeNi-MOF, we performed high-resolution XPS analysis.[42] This advanced surface-sensitive technique enabled precise determination of both elemental distribution and oxidation states at the material's interface. Fig. 6 presented the XPS results of the FeNi-MOF sample, with all spectra fitted using Gaussian–Lorentzian mixed functions.

Fig. 6(a) displayed the XPS full spectrum clearly showing characteristic peaks of five main elements in FeNi-MOF: C, N, O, Fe, and Ni, confirming the successful synthesis of the bimetallic MOF material. The high-resolution C 1s XPS spectrum as shown

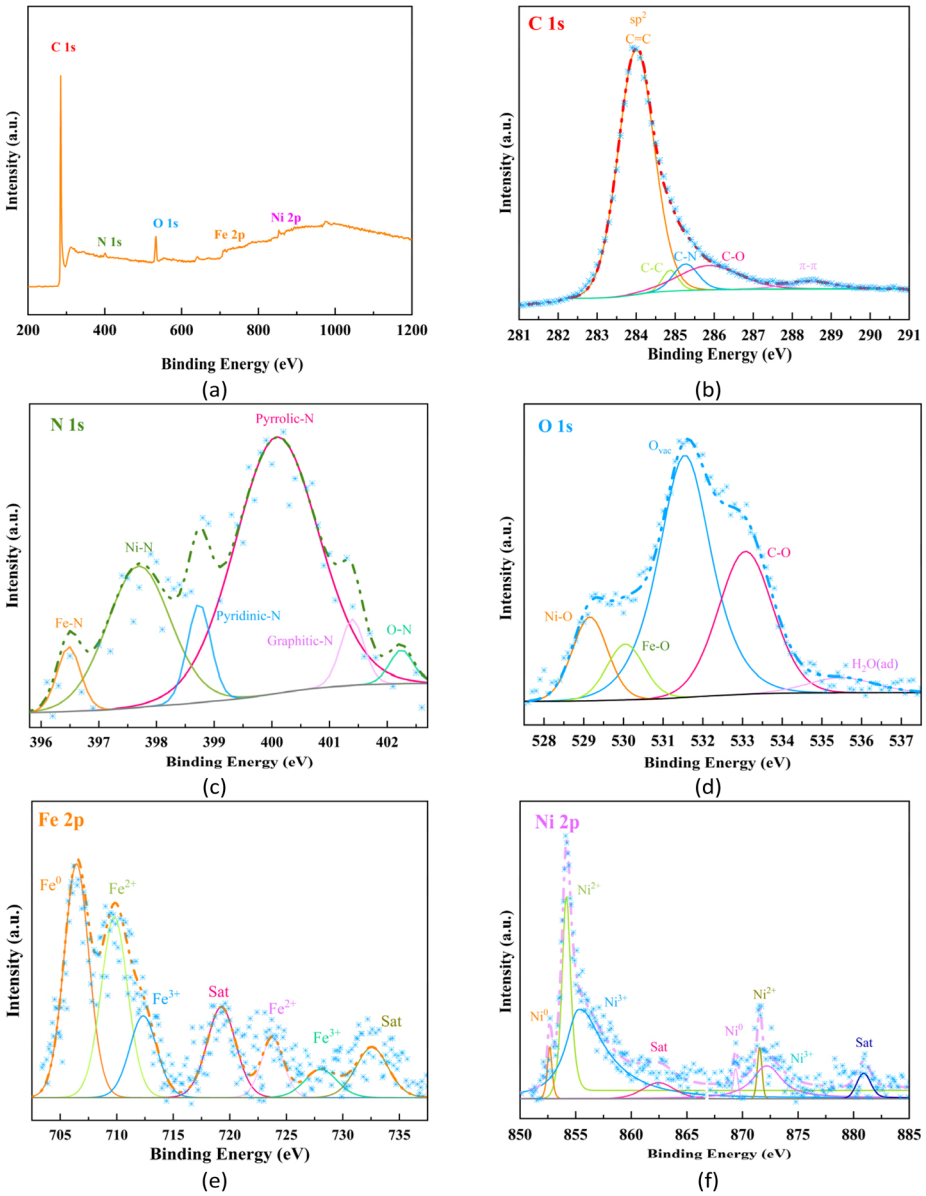

Fig. 6 XPS spectra of FeNi-MOF over the spectral regions: (a) total spectra; (b) C 1s; (c) N 1s; (d) O 1s; (e) Fe 2p; (f) Ni 2p.

in Fig. 6(b) revealed four chemically distinct carbon environments: a dominant peak at 284.0 eV (graphitic sp^2 C=C), accompanied by characteristic signatures at 284.9 eV (aliphatic sp^3 C–C), 285.3 eV (C–N coordination), 285.9 eV (C–O bonding), and 288.4 eV (π–π^* satellite transitions).[43,44] The presence of the C–N peak directly confirmed the successful doping of nitrogen into the carbon framework structure, which was significant for enhancing the acoustic performance of the material.

The deconvoluted N 1s XPS spectrum as shown in Fig. 6(c) demonstrated six chemically distinct nitrogen configurations: metal-coordinated N (396.5 eV, Fe/Ni-Nx), pyridinic-N (397.7 eV, N-6), pyrrolic-N (398.7 eV, N-5), graphitic-N (400.1 eV, N-Q), oxidized-N (401.4 eV, N–O), and N–N dimers (402.2 eV).[45,46] These diverse nitrogen species, especially pyridinic and graphitic nitrogen, exhibited significant interactions in alkaline media.

The deconvoluted O 1s spectrum as shown in Fig. 6(d) resolved four distinct oxygen states in the FeNi-MOF: (i) metal–oxygen coordination centers (529.2 eV for Ni–O and 530.0 eV for Fe–O), (ii) oxygen-deficient sites at 531.5 eV, (iii) carboxylate oxygen (C=O) at 533.1 eV, and (iv) a minor contribution from physisorbed H_2O (535.5 eV).[47,48] This distribution confirmed successful formation of bimetallic coordination networks while revealing defect characteristics.

The deconvoluted Fe 2p XPS spectrum as shown in Fig. 6(e) exhibited multiple splitting features characteristic of iron's oxidation states, with the $2p_{3/2}$ and $2p_{1/2}$ spin–orbit doublets showing distinct satellite structures. Fitting analysis indicated iron existed in three valence states: zero-valent iron (Fe^0) with a $2p_{3/2}$ peak at 706.6 eV, ferrous iron (Fe^{2+}) with $2p_{3/2}$ and $2p_{1/2}$ peaks at 710.0 eV and 723.9 eV, respectively, and ferric iron (Fe^{3+}) with $2p_{3/2}$ and $2p_{1/2}$ peaks at 712.6 eV and 728.4 eV,

respectively.[49] The spectrum further exhibited distinct satellite features at 719.5 eV and 732.8 eV, which were diagnostic of Fe^{3+} species, consistent with reported shake-up transitions in iron oxide systems.[50]

The Ni 2p high-resolution XPS spectrum in Fig. 6(f) similarly showed nickel existing in multiple valence states: zero-valent nickel (Ni^0) with $2p_{3/2}$ and $2p_{1/2}$ peaks at 852.7 eV and 869.4 eV, respectively, divalent nickel (Ni^{2+}) with $2p_{3/2}$ and $2p_{1/2}$ peaks at 854.2 eV and 871.6 eV, respectively, and trivalent nickel (Ni^{3+}) with $2p_{3/2}$ and $2p_{1/2}$ peaks at 855.7 eV and 872.7 eV, respectively. Peaks at 862.6 eV and 881.0 eV were satellite peaks of nickel. This co-existence of multiple valence states of nickel might have resulted from partial oxidation of Ni^{2+} to Ni^{3+} during the material drying process, forming corresponding oxides and nitrides.[51]

The analysis results indicated that FeNi-MOF not only successfully achieved synergistic doping of Fe and Ni dual metals but also formed rich C–N coordination structures and various nitrogen species. Critically, the coexistence of pyridinic-N and graphitic-N moieties, coupled with Fe/Ni multivalent synergism, engendered hierarchical spatial architectures that fundamentally governed the material's exceptional acoustic attenuation capabilities. These microstructural and electronic state characteristics provided a theoretical foundation for explaining the excellent acoustic properties of FeNi-MOF.

3.2. Acoustic characteristics analysis

3.2.1. Acoustic performance of FeNi-MOF@Al-FM with different thicknesses. The acoustic attenuation performance of aluminum foam metals (Al-FM) and their FeNi-MOF composites across varying thicknesses (5–15 mm) were systematically investigated through impedance tube measurements in 100–4000 Hz. The test results revealed significant correlations between material structure and acoustic performance as shown in Fig. 7.

All investigated materials displayed pronounced frequency-dependent acoustic behavior in the 100–1000 Hz range, exhibiting progressively enhanced sound absorption coefficients with increasing frequency.[52,53] Notably, the 15 mm FeNi-MOF@Al-FM composite achieved optimal low-frequency performance, with absorption coefficient rising monotonically from 0.01 (100 Hz) to 0.085 (1000 Hz), demonstrating a 7.5-fold enhancement across this spectral window. Particularly noteworthy was a significant sound absorption peak (approximately 0.09) observed at around 600 Hz, indicating that this material possessed resonant sound absorption characteristics at this frequency.

FeNi-MOF@Al-FM-10 and FeNi-MOF@Al-FM-5 composite materials also exhibited resonance peaks at similar frequencies, but with peak intensities that decreased with reduced thickness. The sound absorption coefficient curve of the single Al-FM-5 material remained relatively flat, showing the lowest sound absorption performance. All materials exhibited a small common peak in the 300–400 Hz range, which might have been attributed to the acoustic characteristics of the testing apparatus itself or the inherent structural features of the aluminum foam metal.

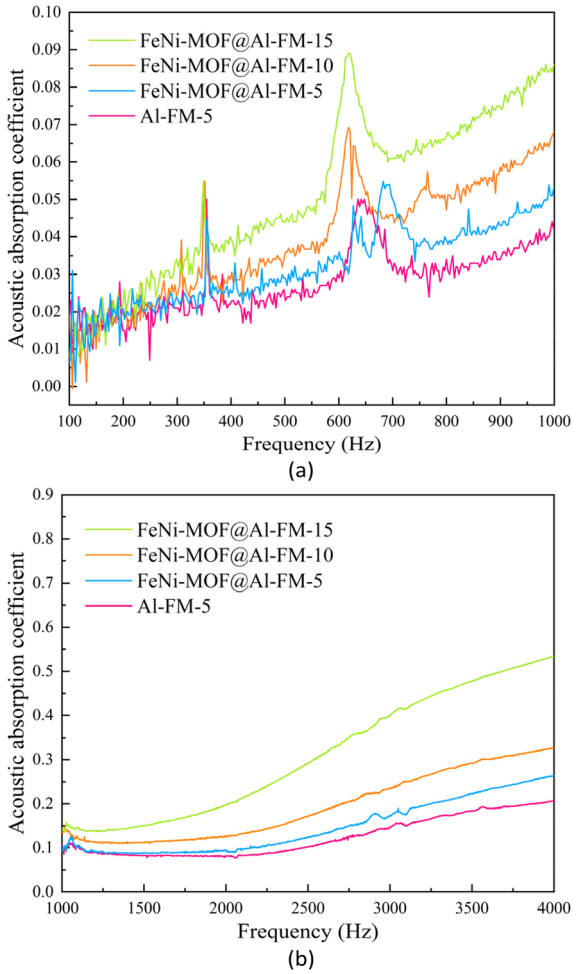

Fig. 7 Acoustic absorption coefficients of FeNi-MOF@Al-FM with different thicknesses: (a) low frequency range; (b) high frequency range.

The double-peak phenomenon observed in the 600–700 Hz range for FeNi-MOF@Al-FM-5 was likely caused by localized resonance coupling effects within the composite material.[36,54] This bimodal structure resulted from the acoustic interaction between MOF nanoparticles and the aluminum foam metal skeleton. The FeNi-MOF nanoparticles, embedded as a dispersed phase within the pores of the aluminum foam, created microscopic heterostructures with distinct acoustic impedances.[55]

The MOF particles (with micropore diameters <2 nm) acted as distributed resonators, generating Helmholtz resonance at their intrinsic frequency (~680 Hz), while the cavity structure of the aluminum foam (mesopore diameters: 100–500 μm) induced localized resonance at a slightly lower frequency (~610 Hz). When the composite thickness was small (5 mm), the sound wave penetration depth was comparable to the material thickness, resulting in weak coupling between these two resonance modes. This allowed them to manifest independently while still interacting, leading to the coexistence of two distinct but closely spaced resonance peaks. The coupling strength depended on the sound wave propagation path and

interfacial reflection characteristics within the finite thickness.[56,57]

As the material thickness increased to 10 mm and 15 mm, the extended propagation path of sound waves within the material enhanced multiple scattering and energy dissipation effects. Consequently, the acoustic coupling between MOF particles and the metal skeleton transitioned from weak to strong coupling. Under strong coupling conditions, the originally independent resonance modes interacted and merged, forming a single broadened resonance peak.[18,58] Furthermore, the increased thickness introduced longer propagation paths and accumulated phase differences, reducing the coherence of localized resonance modes and further promoting the transition from a double-peak to a single-peak profile. This shift from bimodal to unimodal resonance reflected a size-dependent coupling mechanism between localized resonance units and the overall structural resonance in the composite material. These findings provided critical insights for designing sound-absorbing materials with tailored frequency responses.

Material thickness exerted a pronounced influence on acoustic attenuation performance in the high-frequency range (1000–4000 Hz), with thicker specimens demonstrating substantially enhanced sound dissipation capabilities.[59] The sound absorption coefficient of FeNi-MOF@Al-FM-15 increased approximately linearly from 0.15 at 1000 Hz to 0.54 at 4000 Hz, exhibiting the highest high-frequency sound absorption efficiency. The 10 mm and 5 mm FeNi-MOF@Al-FM composites achieved sound absorption coefficients of 0.33 and 0.27 at 4000 Hz, respectively, while unmodified Al-FM-5 demonstrated inferior performance (coefficient = 0.22). All tested materials exhibited gradually increasing, resonance-free absorption curves in high frequencies (1000–4000 Hz), indicating dominant viscous-thermal energy dissipation mechanisms within the porous structures.

Comparative analysis of the sound absorption characteristics of FeNi-MOF@Al-FM composite materials with different thicknesses determined a positive correlation between thickness and sound absorption performance. Increasing the Al-FM thickness from 5 mm to 15 mm substantially enhanced the composites' broadband sound absorption performance, particularly in high frequencies. At 4000 Hz, FeNi-MOF@Al-FM-15 exhibited a 100% greater absorption coefficient (about 0.54) compared to its 5 mm counterpart (about 0.22), while low-frequency improvements remained marginal.

The integration of FeNi-MOF substantially improved the broadband acoustic performance of Al-FM, as evidenced by comparative analysis of Al-FM-5 and FeNi-MOF@Al-FM-5. The MOF-modified composite demonstrated enhanced sound absorption coefficients across all frequencies, with particularly notable gains at 600 Hz (low-frequency resonance) and above 2000 Hz (high-frequency damping). These improvements correlated with the MOF's hierarchical porosity and intrinsic acoustic resonance properties. The results demonstrated that FeNi-MOF@Al-FM composites represented a promising class of acoustic absorbers, particularly the 15 mm variant (FeNi-MOF@Al-FM-15), which achieved exceptional broadband noise reduction. The material synergistically combined low-frequency resonant absorption with high-frequency porous damping, enabling effective attenuation across the entire audible spectrum.

These findings provided important references for further optimizing the design of sound-absorbing materials. By controlling the thickness of aluminum foam metal and the method of MOF incorporation, functional materials with excellent sound absorption performance for specific frequency ranges could be designed.

3.2.2. Acoustic performance of FeNi-MOF@Al-FM with different mass ratios. This research systematically investigated the sound absorption characteristics of composite materials consisting of aluminum foam metal loaded with different mass ratios of MOF (5%, 10%, 20%) at a fixed thickness (5 mm) in the frequency range of 100–4000 Hz, as shown in Fig. 8. Through detailed analysis of the variation of sound absorption coefficients with frequency, the regulatory mechanism of MOF loading mass ratio on the acoustic performance of composite materials and their potential application value were revealed.

Experimental results showed that in the low-frequency region of 100–1000 Hz, all tested samples exhibited frequency-

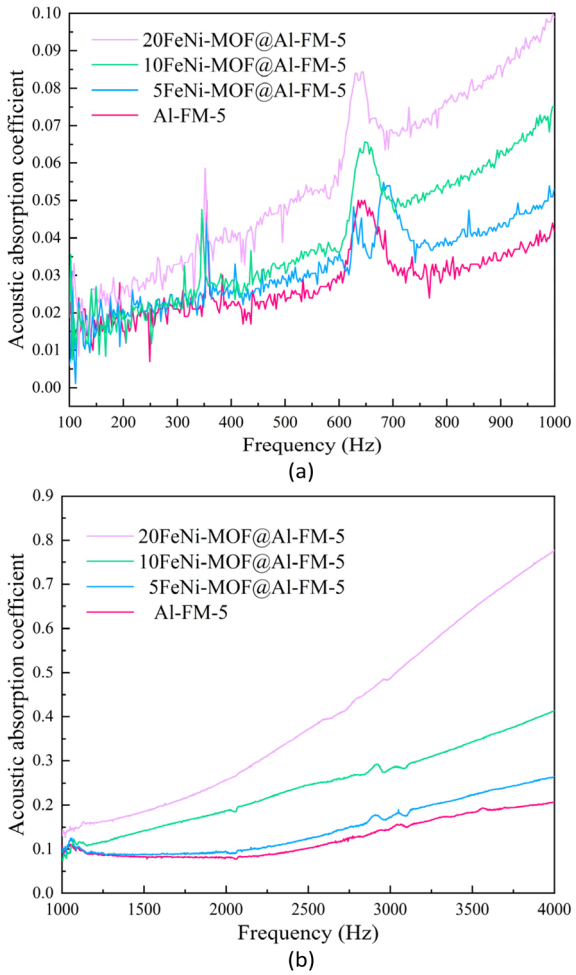

Fig. 8 Acoustic absorption coefficients of FeNi-MOF@Al-FM with different mass ratios: (a) low frequency range; (b) high frequency range.

dependent sound absorption behavior. The 20FeNi-MOF@Al-FM-5 composite exhibited optimal low-frequency acoustic attenuation, showing a 6.5-fold enhancement in sound absorption coefficient from 0.015 (100 Hz) to 0.098 (1000 Hz). The composite demonstrated a pronounced resonance peak at 600 Hz (coefficient ≈ 0.085), followed by monotonic enhancement of acoustic absorption (0.072 to 0.098) across the 800–1000 Hz range.

The 10FeNi-MOF@Al-FM-5 composite exhibited secondary acoustic performance, demonstrating a 600 Hz resonance peak (coefficient ≈ 0.065) and achieving 0.072 at 1000 Hz. In comparison, the 5FeNi-MOF@Al-FM-5 showed reduced absorption capability, with a weaker resonance (coefficient ≈ 0.050) and limited broadband performance (coefficient ≈ 0.051 at 1000 Hz). Unmodified Al-FM-5 displayed the poorest low-frequency attenuation, exhibiting a near-flat absorption profile (coefficient = 0.042 at 1000 Hz) throughout the measured range.

All tested materials exhibited a small common peak around 350 Hz, which might have been related to the acoustic characteristics of the test device or the inherent structural parameters of the aluminum foam metal. Around 600 Hz, different materials exhibited resonant sound absorption behaviors of varying intensities, indicating that the materials had specific resonant sound absorption mechanisms at this frequency, and the resonance intensity was positively correlated with the FeNi-MOF loading mass ratio. As the mass ratio of FeNi-MOF to Al-FM increased from 5% to 20%, the low-frequency resonant sound absorption peak intensity and overall sound absorption performance showed a significant enhancement trend.

The 5FeNi-MOF@Al-FM-5 composite exhibited dual peaks at 610 Hz and 680 Hz in the 600–700 Hz frequency range, while other materials only showed a single peak at approximately 620 Hz. This phenomenon was remarkably similar to the results obtained from thickness-dependent experiments, with essentially identical underlying mechanisms. The dual peaks were primarily attributed to the combined effects of the Helmholtz resonator mechanism from MOF particles and the local structural resonance mode dominated by the aluminum foam skeleton.[55] At low MOF content, the relatively weak acoustic coupling at the material interface allowed both components to maintain their independent resonance characteristics, resulting in two distinct resonance peaks. As the FeNi-MOF mass ratio increased to 10% and 20%, the distribution density of MOF particles within the aluminum foam pores significantly increased, leading to improved acoustic impedance matching at the interface. This enhancement strengthened the resonance coupling effect between the two components. The high-concentration MOF filling modified the overall acoustic impedance characteristics of the composite material, causing the originally independent resonance modes to gradually merge into a single coupled resonance system with a stabilized frequency around 620 Hz. During this transition from bimodal to unimodal behavior, the acoustic performance of the composite material evolved from a superposition effect of local resonators to a unified response of an integrated resonance cavity.[56] These observations clearly demonstrated the regulatory role of interfacial coupling strength in determining the acoustic properties of composite materials.

The high-frequency acoustic performance (1000–4000 Hz) exhibited strong dependence on FeNi-MOF loading concentration, with greater mass ratios yielding substantially enhanced sound attenuation. The 20FeNi-MOF@Al-FM-5 composite material exhibited excellent high-frequency sound absorption capability, with its sound absorption coefficient increasing approximately linearly from 0.15 at 1000 Hz to 0.82 at 4000 Hz. The 10FeNi-MOF@Al-FM-5 composite demonstrated secondary high-frequency attenuation capability (coefficient = 0.43 at 4000 Hz), while the 5FeNi-MOF@Al-FM-5 variant showed intermediate performance (coefficient = 0.28). Unmodified Al-FM-5 exhibited the most limited acoustic damping (coefficient = 0.22), confirming the critical role of MOF loading concentration in high-frequency sound absorption. The sound absorption curves in the high-frequency region generally showed a smooth upward trend, with no obvious resonance peaks observed, indicating that high-frequency sound absorption mainly relied on viscous consumption and thermal loss mechanisms within the porous structure of the material.

Through systematic comparison of composite materials with different MOF loading mass ratios, a quantitative relationship between loading mass ratio and sound absorption performance was established. Systematic enhancement of broadband acoustic performance was observed with increasing FeNi-MOF loading from 5 to 20 wt%, particularly in high-frequency range. The 20 wt% composite achieved a 2.9-fold greater absorption coefficient of 0.82 at 4000 Hz compared to its 5 wt% counterpart (coefficient = 0.28), demonstrating concentration-dependent acoustic optimization. The regulatory effect of FeNi-MOF loading mass ratio on high-frequency sound absorption performance was significantly greater than its effect on low frequencies, with differences in sound absorption coefficients of materials with different loading mass ratios reaching 0.6 at 4000 Hz, while the difference at 600 Hz was only about 0.035.

As the FeNi-MOF loading increased, the improvement in sound absorption performance exhibited a non-linear relationship. When the mass ratio increased from 5% to 10%, the high-frequency 4000 Hz sound absorption performance improved by approximately 53%; while from 10% to 20%, the improvement was about 91%. This phenomenon suggested the possible existence of a critical loading amount, beyond which the improvement in sound absorption performance became more significant, providing an important reference for optimizing composite material design.

3.3. Sound absorption mechanism analysis

To elucidate the influence of MOFs on the macroscopic acoustic properties of materials, the Johnson–Champoux–Allard (JCA) parameter model is established in this research, which currently represents the most accurate generalized acoustic model for characterizing the sound absorption properties of rigid-frame porous metallic materials across a broad frequency range.[60,61] The JCA model, combining the advantages of both

Johnson–Allard and Champoux–Allard models, describes sound transmission in porous materials by considering acoustic wave propagation and absorption mechanisms, enabling the prediction of sound absorption performance. In the JCA model, sound propagation occurs through two primary mechanisms: intra-pore and inter-pore wave transmission.[62,63] The model assumes porous materials consist of interconnected pores and solid pore walls, with key macroscopic acoustic parameters including porosity (ϕ), tortuosity (χ), characteristic length (d), and acoustic impedance.

The porosity was calculated as:[64]

$$\phi = \left(1 - \frac{\rho_m}{\rho_b}\right) \times 100\% \quad (11)$$

where ρ_m and ρ_b represented the composite and strut densities, respectively.

For 5FeNi-MOF@Al-FM-5 and 20FeNi-MOF@Al-FM-5, the porosities were calculated as 82.76% and 83.21%, respectively, based on measured densities (FeNi-MOF: packing density 0.22 g cm^{-3}, strut density 1.81 g cm^3; Al-FM: block density 0.47 g cm^{-3}, strut density 2.70 g cm^{-3}).

Tortuosity was derived from porosity using

$$\chi = 2 + 2\cos\left[\frac{4\pi}{3} + \frac{1}{3}\cos^{-1}(2\phi - 1)\right] \quad (12)$$

yielding values of 1.528 and 1.520 for the 5% and 20% MOF-loaded composites, respectively.

The characteristic representative unit cell (RUC) dimension was determined by

$$d = \frac{3(3-\chi)(\chi-1)}{3.18\frac{w}{l^2} - 0.61\frac{w^2}{l^3}} \quad (13)$$

where l and w represented the opening side length and matrix skeleton width, respectively, as measured from electron microscopy as shown in Fig. 9 (5% MOF: l = 28.21 μm, w = 87.62 μm; 20% MOF: l = 45.50 μm, w = 99.58 μm). This yielded RUC dimensions of 212.68 μm and 173.52 μm for the respective composites.

Fluid permeability (K) and flow resistivity (σ) were calculated as

$$K = \frac{\phi^2 d^2}{36\chi(\chi-1)} \quad (14)$$

$$\sigma = \frac{\mu}{K} \quad (15)$$

where μ was the viscosity of air at 25 °C with a value of 1.84 × 10^{-5} N s m^{-2}, resulting in permeabilities of 1066.38 m^2 and 732.05 m^2, and flow resistivities of 17 254 Pa s m^{-2} and 25 135 Pa s m^{-2} for the 5% and 20% MOF composites. The incorporation of FeNi-MOF strongly enhanced the fluid contact area. Thus, the increase in flow friction at solid–liquid interfaces leads to larger amount of energy dissipation when sound travels through the structure.

The composite's acoustic attenuation was governed by two mechanisms:[65,66] (1) low-frequency resonance absorption (<1000 Hz) from structural vibration modes, and (2) high-frequency porous damping (>2000 Hz) through viscothermal energy conversion. The viscothermal absorption mechanism involves viscous and thermal boundary layer effects near pore walls, where velocity and temperature gradients convert acoustic energy to heat through viscous friction and thermal conduction.

A characteristic resonance peak at ~630 Hz originated from microstructural features formed by FeNi-MOF particles and Al-FM framework, with efficiency positively correlating with MOF loading due to increased resonance units. In 5 mm-thick samples, limited material thickness restricted cumulative boundary layer effects, making viscothermal dissipation localized in MOF micropores (<2 nm, complete viscous domination) and Al-FM mesopores (100–500 μm, boundary layer-limited dissipation).

Thicker samples exhibited enhanced viscothermal absorption through:[67,68] (1) increased pore channel complexity generating turbulent flows, and (2) prolonged propagation paths amplifying boundary layer effects. At low MOF loading (5%), discrete "island" distributions of MOF particles created localized high-dissipation zones with bypass routes, as shown in Fig. 2(c), limiting overall efficiency. The 20% MOF loading formed continuous networks establishing a hierarchical pore system (mm-scale Al-FM macropores → μm-scale MOF interparticle voids → nm-scale MOF intrinsic pores), as shown in Fig. 2(e), enabling progressive energy dissipation through three-length-scale filtration.

This transition from bimodal to unimodal behavior reflected a shift from superimposed local resonators to unified cavity response, demonstrating interface coupling's regulatory role. High-frequency dissipation (2000–4000 Hz) occurred through coupled viscous friction at gas–solid interfaces and thermal conduction in tortuous pores.[69] The multi-scale pore architecture (nm to mm) provided matched dissipation channels across frequencies: Al-FM mesopores dominated 2000–3000 Hz, while MOF micropores controlled 3000–4000 Hz absorption.

The exceptional high-frequency performance stemmed from FeNi-MOF's intrinsic properties: ultrahigh specific surface area (1000–1500 m^2 g^{-1}) and tunable nanoporosity. Abundant interfaces provided vast dissipation areas, while precisely

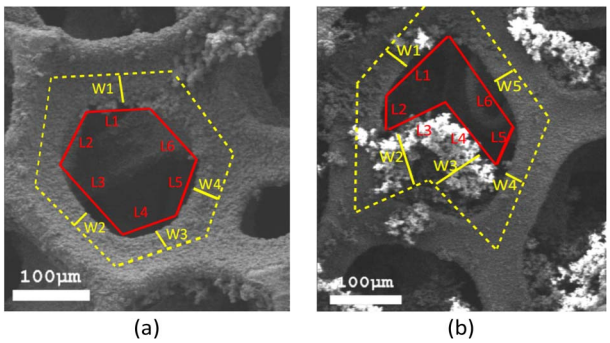

Fig. 9 SEM image demonstrates the measurement of side length l and side width w of FeNi-MOF@Al-FM: (a) 5FeNi-MOF@Al-FM-5; (b) 20FeNi-MOF@Al-FM-5.

adjustable pore sizes enabled frequency-selective absorption matching boundary layer thicknesses. Heterogeneous interfaces between MOF and Al-FM created additional dissipation sites through scattering, reflection, and mode conversion, with surface roughness and chemical heterogeneity further enhancing losses.

Increasing MOF loading created more complex hierarchical pores, generating synergistic effects for broadband absorption. The optimized 20FeNi-MOF@Al-FM-5 composite achieved a peak absorption coefficient of 0.82 at 4000 Hz, demonstrating exceptional performance in the crucial 2000–4000 Hz range for practical noise control applications. This work establishes a viable strategy for designing next-generation acoustic materials through precise MOF/metal foam ratio control.

From an application perspective, the efficient viscothermal sound absorption performance made the FeNi-MOF@Al-FM composite particularly suitable for broadband acoustic applications. In architectural acoustics, this material could be employed in demanding environments such as concert halls and recording studios, where its broadband absorption characteristics effectively mitigated standing waves and echoes to create optimal acoustic environments. For transportation noise reduction, the composite's lightweight properties rendered it ideal for weight-sensitive applications in aerospace and high-speed rail systems.

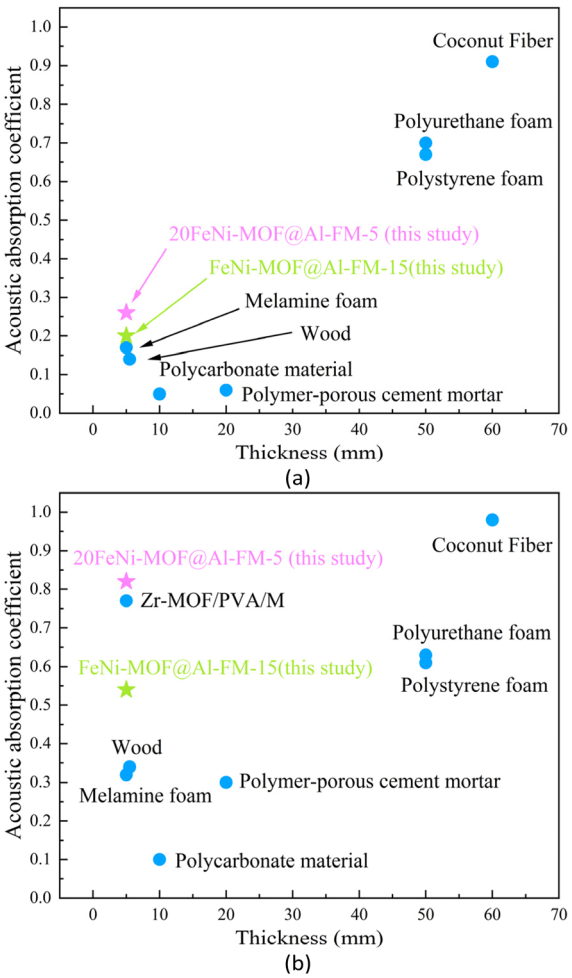

Fig. 10 Sound absorption performance comparative analysis of FeNi-MOF@Al-FM composite *vs.* conventional materials: (a) sound absorption coefficient at 2000 Hz; (b) sound absorption coefficient at 4000 Hz.

Fig. 10 presented a comparative analysis of sound absorption coefficients between the FeNi-MOF@Al-FM composite and conventional architectural absorbers (melamine foam,[55] polystyrene foam,[70] polyurethane foam,[71] polycarbonate material,[72] Zr-MOF/PVA/M,[55] coconut fiber,[9] wood,[73] polymer-porous cement mortar[74]). The developed composite demonstrated exceptional acoustic attenuation performance in high-frequency regions. While conventional wisdom suggested that thicker materials were typically required to achieve sufficient energy dissipation through increased surface area, the FeNi-MOF@Al-FM composite surprisingly exhibited superior acoustic attenuation at significantly reduced thicknesses compared to standard absorbers like polyurethane foam, mineral wool, wood, and natural fibers. Remarkably, at 4000 Hz, the composite achieved sound absorption coefficients more than double those of melamine foam. This ultrathin FeNi-MOF@Al-FM composite demonstrated substantial application potential for both architectural and transportation sectors.

The material's exceptional performance was attributed to its unique hierarchical pore structure, which enabled efficient viscothermal energy conversion across multiple length scales. Unlike traditional absorbers that relied primarily on thickness-dependent dissipation mechanisms, the composite's nano–micro–macro pore architecture facilitated broadband absorption through optimized interfacial interactions and boundary layer effects. This breakthrough in thin-film acoustic material design addressed critical challenges in space-constrained applications where conventional thick absorbers proved impractical.

4. Conclusions

This study developed FeNi-MOF@Al-FM composite materials with optimized acoustic performance through structural engineering. SEM analysis revealed that increasing FeNi-MOF loading (0–20 wt%) enhanced surface particle density while maintaining open channels, forming semi-open porous architectures. The hexagonal spindle-like FeNi-MOF crystals exhibited MIL-88(Fe)-type structure confirmed by XRD, with peak shifts indicating successful Ni doping. FTIR and XPS verified characteristic functional groups (N–H, C–O, Fe–O) and confirmed bimetallic coordination environments. TGA demonstrated three-stage thermal degradation involving solvent loss, ligand decomposition, and framework collapse.

Acoustic testing revealed thickness-dependent performance, with 15 mm samples achieving optimal broadband absorption. The composite displayed dual absorption mechanisms: low-frequency resonance ($\approx$600 Hz) from MOF-framework interactions, and high-frequency viscous/thermal dissipation through hierarchical porosity. Notably, 20FeNi-MOF@Al-FM-5 (20% loading, 5 mm thickness) exhibited exceptional performance with 0.82 absorption coefficient at 4000 Hz – 3.7$\times$ enhancement

over unmodified Al-FM. The synergy between MOFs' nanoscale pores (high surface area) and Al-FM's macroporous structure enabled full-spectrum sound attenuation.

Structure–performance relationships established that acoustic properties could be tuned through thickness control and MOF loading optimization. The composite's multi-scale porosity (nano-to-macro) combined with bimetallic coordination effects facilitated simultaneous resonant absorption and broadband dissipation. These findings provide a design blueprint for advanced acoustic materials, particularly valuable in noise control applications requiring thin-profile solutions with full-frequency effectiveness. The material demonstrates significant potential for architectural acoustics, precision instrument protection, and industrial noise mitigation, offering a balanced combination of structural stability, thermal resistance, and tunable sound absorption performance.

Data availability

The data supporting the findings of this study are available within the article. Additional datasets generated and analyzed during the current study are available from the corresponding author upon request.

Author contributions

Conceptualization, Y. G. and D. W.; methodology, J. G. and D. W.; validation, J. G. and X. Z.; formal analysis, Y. G. and Y. G.; investigation, Y. G. and X. Z.; resources, Y. G. and G. T.; data curation, Y. G.; writing—original draft, Y. G.; writing—review & editing, Y. G.; supervision, G. T.; project administration, Y. G.; funding acquisition, Y. G. All authors have read and agreed to the published version of the manuscript.

Conflicts of interest

There are no conflicts to declare.

Acknowledgements

Financial supports received from “Chunhui Plan cooperative scientific research project of the Ministry of Education of China (HZKY20220498); Shandong Enterprise Technology Innovation Project Plan (2024637010001092); Shandong Province Technology Innovation Project Plan (202360001105, 202350101441); Shandong Province Housing and Urban-Rural Construction Science and Technology Project (2022-K7-11, 2021-K8-10, 2020-K2-10).

References

1 P. Liang, Y. P. Fu and K. Z. Gao, Multi-product disassembly line balancing optimization method for high disassembly profit and low energy consumption with noise pollution constraints, *Eng. Appl. Artif. Intell.*, 2024, **130**, 107721, DOI: **10.1016/j.engappai.2023.107721**.

2 M. Y. Shams, T. Abd El-Hafeez and E. Hassan, Acoustic data detection in large-scale emergency vehicle sirens and road noise dataset, *Expert Syst. Appl.*, 2024, **249**, 123608, DOI: **10.1016/j.eswa.2024.123608**.

3 O. Hahad, M. Kuntic, S. Al-Kindi, I. Kuntic, D. Gilan, K. Petrowski, A. Daiber and T. Münzel, Noise and mental health: evidence, mechanisms, and consequences, *J. Exposure Sci. Environ. Epidemiol.*, 2025, **35**, 16–23, DOI: **10.1038/s41370-024-00642-5**.

4 A. Arjunan, A. Baroutaji, J. Robinson, A. Vance and A. Arafat, Acoustic metamaterials for sound absorption and insulation in buildings, *Build Environ.*, 2024, **251**, 111250, DOI: **10.1016/j.buildenv.2024.111250**.

5 H. Q. Liu and F. J. Wang, A novel semi-analytical meshless method for the thickness optimization of porous material distributed on sound barriers, *Appl. Math. Lett.*, 2024, **147**, 108844, DOI: **10.1016/j.aml.2023.108844**.

6 M. Ravanbod, S. Ebrahimi-Nejad and M. Mollajafari, A thin-walled cavity structure with double-layer tapered scatterer locally resonant metamaterial plates for extreme low-frequency attenuation, *Int. J. Solids Struct.*, 2024, **293**, 112742, DOI: **10.1016/j.ijsolstr.2024.112742**.

7 L. L. Chen, H. Lian, S. Natarajan, W. Zhao, X. Y. Chen and S. P. A. Bordas, Multi-frequency acoustic topology optimization of sound-absorption materials with isogeometric boundary element methods accelerated by frequency-decoupling and model order reduction techniques, *Comput. Methods Appl. Mech. Eng.*, 2022, **395**, 114997, DOI: **10.1016/j.cma.2022.114997**.

8 S. Mehrzad, E. Taban, P. Soltani, S. E. Samaei and A. Khavanin, Sugarcane bagasse waste fibers as novel thermal insulation and sound-absorbing materials for application in sustainable buildings, *Build Environ.*, 2022, **211**, 108753, DOI: **10.1016/j.buildenv.2022.108753**.

9 U. Berardi and G. Iannace, Acoustic characterization of natural fibers for sound absorption applications, *Build Environ.*, 2015, **94**, 840–852, DOI: **10.1016/j.buildenv.2015.05.029**.

10 S. Ma, A. Li and L. G. Pan, Application Progress of Multi-Functional Polymer Composite Nanofibers Based on Electrospinning: A Brief Review, *Polymers*, 2024, **16**(17), 2459, DOI: **10.3390/polym16172459**.

11 S. Dong, Y. Y. Duan, X. Y. Chen, F. You, X. L. Jiang, D. R. Wang, D. D. Hu and P. Zhao, Recent Advances in Preparation and Structure of Polyurethane Porous Materials for Sound Absorbing Application, *Macromol. Rapid Commun.*, 2024, **45**(14), e2400108, DOI: **10.1002/marc.202400108**.

12 Z. Kamble, Advanced structural and multi-functional sandwich composites with prismatic and foam cores: A review, *Polym. Compos.*, 2024, **45**, 16355–16382, DOI: **10.1002/pc.27849**.

13 C. C. Zhang, H. Q. Li, J. X. Gong, J. H. Chen, Z. Li, Q. J. Li, M. L. Cheng, X. Li and J. F. Zhang, The review of fiber-based sound-absorbing structures, *Text. Res. J.*, 2023, **93**, 434–449, DOI: **10.1177/00405175221084736**.

14 M. Amran, R. Fediuk, G. Murali, N. Vatin and A. Al-Fakih, Sound-Absorbing Acoustic Concretes: A Review, *Sustainability*, 2021, **13**(19), 10712, DOI: 10.3390/su131910712.

15 L. He, D. Li, L. Song, J. Fang, H. Li and X. Liu, Biomass aerogel with double layer heterostructure for sound absorption and sound insulation, *Compos. Struct.*, 2025, **359**, 119030, DOI: 10.1016/j.compstruct.2025.119030.

16 M. Yuan, X. Sheng, Z. Cao, Z. Pang and G. Huang, Joint acoustic energy harvesting and noise suppression using deep-subwavelength acoustic device, *Smart Mater. Struct.*, 2020, **29**, 035012, DOI: 10.1088/1361-665X/ab6697.

17 P. Bai, X. Shen, X. Zhang, X. Yang, Q. Yin and A. Liu, Influences of Compression Ratios on Sound Absorption Performance of Porous Nickel–Iron Alloy, *Metals*, 2018, **8**, 539, DOI: 10.3390/met8070539.

18 X. Shen, P. Bai, X. Yang, X. Zhang and S. To, Low Frequency Sound Absorption by Optimal Combination Structure of Porous Metal and Microperforated Panel, *Appl. Sci.*, 2019, **9**, 1507, DOI: 10.3390/app9071507.

19 J. Li, Y. M. Yousry, P. C. Lim, S. Ramakrishna and K. Yao, Mechanism of airborne sound absorption through triboelectric effect for noise mitigation, *Nat. Commun.*, 2024, **15**, 9408, DOI: 10.1038/s41467-024-53847-5.

20 M. Yuan, Z. Cao, J. Luo and X. Chou, Recent Developments of Acoustic Energy Harvesting: A Review, *Micromachines*, 2019, **10**, 48, DOI: 10.3390/mi10010048.

21 P.-F. Zhang, Z.-H. Li, Y.-J. Zhou, Q.-F. Zhang, B. Liu, F. Liu, S.-C. Pei, K. Shi and P.-k. Bai, Improved sound absorption with 3D-printed micro-perforated sandwich structures, *J. Mater. Res. Technol.*, 2025, **34**, 855–865, DOI: 10.1016/j.jmrt.2024.12.082.

22 M. Yuan, W. Yao, Z. Ding, J. Li, B. Dai, X. Zhang and Y. Xie, Integrated acoustic metamaterial triboelectric nanogenerator for joint low-frequency acoustic insulation and energy harvesting, *Nano Energy*, 2024, **122**, 109328, DOI: 10.1016/j.nanoen.2024.109328.

23 M. Yuan, B. Zhu, Q. Jiang, Y. Xie and R. Ohayon, Multifunctional subwavelength device for wide-band sound absorption and acoustic-electric conversion, *Sens. Actuators, A*, 2025, **389**, 116554, DOI: 10.1016/j.sna.2025.116554.

24 F. Feng, C. He, Z. Cui, T. Ying, J. Cai and M. Tao, Topology optimization of multi-material underwater broadband sound absorption metamaterial based on genetic algorithm, *J. Acoust. Soc. Am.*, 2025, **157**, 3482–3496, DOI: 10.1121/10.0036637.

25 M. Yuan, W. Yu, Y. Jiang, Z. Ding, Z. Zhang, X. Zhang and Y. Xie, Triboelectric nanogenerator metamaterials for joint structural vibration mitigation and self-powered structure monitoring, *Nano Energy*, 2022, **103**, 107773, DOI: 10.1016/j.nanoen.2022.107773.

26 Y. L. Hou, C. Y. Yang, Z. J. Yang, H. Q. Zhou, L. M. Guo, J. Guo and X. F. Zhang, Building robust metal-organic frameworks with premade ligands, *Coord. Chem. Rev.*, 2024, **505**, 215690, DOI: 10.1016/j.ccr.2024.215690.

27 S. H. Zhou, L. Shi, Y. Z. Li, T. Yang and S. L. Zhao, Metal-Organic Framework-Based Electrocatalysts for Acidic Water Splitting, *Adv. Funct. Mater.*, 2024, **34**(34), 2400767, DOI: 10.1002/adfm.202400767.

28 C. Li, Y. Q. Yuan, M. Yue, Q. W. Hu, X. P. Ren, B. C. Pan, C. Zhang, K. B. Wang and Q. C. Zhang, Recent Advances in Pristine Iron Triad Metal-Organic Framework Cathodes for Alkali Metal-Ion Batteries, *Small*, 2024, **20**(23), 2310373, DOI: 10.1002/smll.202310373.

29 V. Martinez, T. Stolar, B. Karadeniz, I. Brekalo and K. Uzarevic, Advancing mechanochemical synthesis by combining milling with different energy sources, *Nat. Rev. Chem.*, 2023, **7**, 51–65, DOI: 10.1038/s41570-022-00442-1.

30 I. Ahmed, G. Lee, H. J. Lee and S. H. Jhung, Adsorption of pharmaceuticals from water using metal-organic frameworks (MOFs), MOF-derived carbons, covalent-organic frameworks (COFs), COF-derived carbons: Comparison of the four adsorbents, *Chem. Eng. J.*, 2024, **488**, 151022, DOI: 10.1016/j.cej.2024.151022.

31 R. U. Rajesh, T. Mathew, H. Kumar, A. Singhal and L. Thomas, Metal-organic frameworks: Recent advances in synthesis strategies and applications, *Inorg. Chem. Commun.*, 2024, **162**, 112223, DOI: 10.1016/j.inoche.2024.112223.

32 X. T. Pan, Z. Z. Huang, J. Guo, Q. Y. Wu, C. H. Wang, H. Y. Zhang, J. Zhang and H. Y. Liu, MOF-Derived Nanoparticles with Enhanced Acoustical Performance for Efficient Mechano-Sonodynamic Therapy, *Adv. Mater.*, 2024, **36**(33), 2400142, DOI: 10.1002/adma.202400142.

33 T. F. Zheng, C. P. Xu and Q. Y. Yang, The effect of high-frequency acoustic wave vibration pattern on HKUST's multi-level pore structure, *Ultrason. Sonochem.*, 2023, **95**, 106368, DOI: 10.1016/j.ultsonch.2023.106368.

34 S. S. M. Ameen and K. M. Omer, Recent Advances of Bimetallic-Metal Organic Frameworks: Preparation, Properties, and Fluorescence-Based Biochemical Sensing Applications, *ACS Appl. Mater. Interfaces*, 2024, **16**, 31895–31921, DOI: 10.1021/acsami.4c06931.

35 L. Chang, A. Jiang, M. Rao, F. Ma, H. Huang, Z. Zhu, Y. Zhang, Y. Wu, B. Li and Y. Hu, Progress of low-frequency sound absorption research utilizing intelligent materials and acoustic metamaterials, *RSC Adv.*, 2021, **11**, 37784–37800, DOI: 10.1039/D1RA06493B.

36 W. W. S. Ma, H. Yang, Y. J. Zhao, X. W. Li, J. H. Ding, S. Qu, Q. Y. Liu, Z. X. Hu, R. Li, Q. Q. Tao, *et al.*, Multi-Physical Lattice Metamaterials Enabled by Additive Manufacturing: Design Principles, Interaction Mechanisms, and Multifunctional Applications, *Advanced Science*, 2025, **12**(8), 2405835, DOI: 10.1002/advs.202405835.

37 L. Su, Q. Wang, P. Xiang, D. Yin, X. Ding, L. Liu and X. Zhao, Development of nitrile rubber/eucommia ulmoides gum composites for controllable dynamic damping and sound absorption performance, *RSC Adv.*, 2022, **12**, 21503–21511, DOI: 10.1039/D2RA03597A.

38 J. C. Ji, Q. Luo and K. Ye, Vibration control based metamaterials and origami structures: A state-of-the-art

review, *Mech. Syst. Signal Process.*, 2021, **161**, 107945, DOI: 10.1016/j.ymssp.2021.107945.

39 J. Y. Song, Y. Y. Yu, X. S. Han, W. S. Yang, W. B. Pan, S. J. Jian, G. G. Duan, S. H. Jiang and J. P. Hu, Novel MOF(Zr)-on-MOF(Ce) adsorbent for elimination of excess fluoride from aqueous solution, *J. Hazard. Mater.*, 2024, **463**, 132843, DOI: 10.1016/j.jhazmat.2023.132843.

40 J. Guo, Y. Gao, X. Cao, L. Li, X. Yu, S. Chi, H. Liu, G. Tian and X. Zhao, Ni/N co-doped NH_2-MIL-88(Fe) derived porous carbon as an efficient electrocatalyst for methanol and water co-electrolysis, *Renewable Energy*, 2025, **244**, 122661, DOI: 10.1016/j.renene.2025.122661.

41 X. Cao, Y. Gao, Y. Li, D. M. Weragoda, G. Tian, W. Zhang, Z. Zhang, X. Zhao and B. Chen, Research progress on MOFs and their derivatives as promising and efficient electrode materials for electrocatalytic hydrogen production from water, *RSC Adv.*, 2023, **13**, 24393–24411, DOI: 10.1039/D3RA04110G.

42 Y. Gao, H. Dou, Y. Ma, G. Tian, D. M. Weragoda, S. Li, X. Yang, Z. Zhang, G. Fan and B. Chen, Antibacterial performance effects of Ag NPs *in situ* loaded in MOFs nano-supports prepared by post-synthesis exchange method, *J. Environ. Chem. Eng.*, 2024, **12**, 112133, DOI: 10.1016/j.jece.2024.112133.

43 C. Li, W. Zhang, Y. Y. Cao, J. Y. Ji, Z. C. Li, X. Han, H. W. Gu, P. Braunstein and J. P. Lang, Interfacial Electronic Interactions Between Ultrathin NiFe-MOF Nanosheets and Ir Nanoparticles Heterojunctions Leading to Efficient Overall Water Splitting, *Advanced Science*, 2024, **11**(28), 2401780, DOI: 10.1002/advs.202401780.

44 Y. Li, Y. Gao, X. Cao, X. Rong, B. Chen, G. Tian, Z. Zhu, X. Zhao and Z. Zhang, Encapsulation and thermal properties of composite phase change materials based on cobalt/nitrogen double-doped ZIF-67 derived carbon, *RSC Adv.*, 2023, **13**, 26907–26917, DOI: 10.1039/d3ra04002j.

45 Q. Wang, H. Zhou, J. Y. Qian, B. Xue, H. Du, D. R. Hao, Y. Ji and Q. Li, Ti_3C_2-assisted construction of Z-scheme MIL-88A(Fe)/Ti_3C_2/RF heterojunction: Multifunctional photocatalysis-in-situ-self-Fenton catalyst, *J. Mater. Sci. Technol.*, 2024, **190**, 67–75, DOI: 10.1016/j.jmst.2023.11.045.

46 X. Rong, Q. Cao, Y. Gao, X. Du, H. Dou, M. Yan, S. Li, Q. Wang, Z. Zhang and B. Chen, Performance optimization and kinetic analysis of HNO_3 coupled with microwave rapidly modified coconut shell activated carbon for VOCs adsorption, *Front. Energy Res.*, 2023, **10**, 1047254, DOI: 10.3389/fenrg.2022.1047254.

47 J. Guo, Y. Gao, X. Cao, X. Rong, S. Chi, G. Fan, L. Zhang, G. Tian and X. Zhao, Fe-Co bimetallic MOF-derived carbon directly application as an efficient electrocatalyst for oxygen evolution reaction, *Inorg. Chem. Commun.*, 2024, 113394, DOI: 10.1016/j.inoche.2024.113394.

48 X. Rong, Q. Cao, Y. Gao, T. Luan, Y. Li, Q. Man, Z. Zhang and B. Chen, Synergistic Catalytic Performance of Toluene Degradation Based on Non-Thermal Plasma and Mn/Ce-Based Bimetal-Organic Frameworks, *Molecules*, 2022, **27**, 7363, DOI: 10.3390/molecules27217363.

49 Y. Gao, X. Peng, Z. Zhang, W. Zhang, H. Li, B. Chen, S. Li, Y. Zhang and S. Chi, Ternary mixed-oxide synergy effects of nano TiO_2-Fe_xO_y-MOk (M = Mn, Ce, Co) on alpha-pinene catalytic oxidation process assisted by nonthermal plasma, *Mater. Res. Express*, 2021, **8**, 015509, DOI: 10.1088/2053-1591/abdbf7.

50 Y. Gao, Q. Cao, N. Guan, Z. Zhang, G. Fan, H. Dou, S. Li, Q. Wang and B. Chen, Metal-Organic Framework Supporting Fe_3O_4 Prepared by Microwave in Couple with NTP to Eliminate VOCs from Biofuel, *Front. Energy Res.*, 2022, **10**, 936493, DOI: 10.3389/fenrg.2022.936493.

51 W. Q. Zou, Y. X. Zhou, S. Zhong, F. Liao, J. Lu, L. Y. Zhang and D. P. Sun, Biomimetic FeNi-MOF assisted intelligent theranostic hydrogels for pH identification and treatment of wounds, *Chem. Eng. J.*, 2024, **497**, 154945, DOI: 10.1016/j.cej.2024.154945.

52 Y. F. Zhang, Z. Y. Zhu, Z. H. Sheng, Y. J. He and G. Wang, Sound absorption properties of the metamaterial curved microperforated panel, *Int. J. Mech. Sci.*, 2024, **268**, 109003, DOI: 10.1016/j.ijmecsci.2024.109003.

53 W. F. Kong, T. Fu and T. Rabczuk, Improvement of broadband low-frequency sound absorption and energy absorbing of arched curve Helmholtz resonator with negative Poisson's ratio, *Appl. Acoust.*, 2024, **221**, 110011, DOI: 10.1016/j.apacoust.2024.110011.

54 L. Li, Z. Guo, F. Yang, P. Li, M. Zhao and Z. Zhong, Additively manufactured acoustic-mechanical multifunctional hybrid lattice structures, *Int. J. Mech. Sci.*, 2024, **269**, 109071, DOI: 10.1016/j.ijmecsci.2024.109071.

55 Y.-C. Lan, S. Kamal, C.-C. Lin, Y.-H. Liu and K.-L. Lu, Ultra-thin Zr-MOF/PVA/Melamine composites with remarkable sound attenuation effects, *Microporous Mesoporous Mater.*, 2023, **360**, 112668, DOI: 10.1016/j.micromeso.2023.112668.

56 Y. Sun, Y. Chu, W. Wu and H. Xiao, Nanocellulose-based lightweight porous materials: A review, *Carbohydr. Polym.*, 2021, **255**, 117489, DOI: 10.1016/j.carbpol.2020.117489.

57 P. Zhang, Z. Li, B. Liu, Y. Zhou, M. Zhao, G. Sun, S. Pei, X. Kong and P. Bai, Sound absorption performance of micro-perforated plate sandwich structure based on triply periodic minimal surface, *J. Mater. Res. Technol.*, 2023, **27**, 386–400, DOI: 10.1016/j.jmrt.2023.09.237.

58 M. Askari, D. A. Hutchins, P. J. Thomas, L. Astolfi, R. L. Watson, M. Abdi, M. Ricci, S. Laureti, L. Nie, S. Freear, *et al.*, Additive manufacturing of metamaterials: A review, *Addit. Manuf.*, 2020, **36**, 101562, DOI: 10.1016/j.addma.2020.101562.

59 H. Y. Zhang, H. L. Wang, T. Wang, S. H. Han, X. Zhang, J. Wang and G. H. Sun, Polyurethane Foam with High-Efficiency Flame Retardant, Heat Insulation, and Sound Absorption Modified By Phosphorus-Containing Graphene Oxide, *ACS Appl. Polym. Mater.*, 2024, **6**, 1878–1890, DOI: 10.1021/acsapm.3c02706.

60 Y. Yang, S. Liu, Y. Li, T. Gao, Y. Pan, Y. Li and Y. Jin, Broadband low-frequency sound absorption of multifunctional composite metastructure, *Sci. China: Technol. Sci.*, 2025, **68**, 1220206, DOI: 10.1007/s11431-023-2644-7.

61 X. Zhang, Z. Qu and H. Wang, Engineering Acoustic Metamaterials for Sound Absorption: From Uniform to Gradient Structures, *iScience*, 2020, **23**, 101110, DOI: 10.1016/j.isci.2020.101110.

62 E. Ogam, C. Depollier and Z. E. A. Fellah, The direct and inverse problems of an air-saturated porous cylinder submitted to acoustic radiation, *Rev. Sci. Instrum.*, 2010, **81**, 094902, DOI: 10.1063/1.3482015.

63 V. Langlois, High-frequency permeability of porous media with thin constrictions. I. Wedge-shaped porous media, *Phys. Fluids*, 2022, **34**, 077119, DOI: 10.1063/5.0086257.

64 W. Zhai, X. Yu, X. Song, L. Y. L. Ang, F. Cui, H. P. Lee and T. Li, Microstructure-based experimental and numerical investigations on the sound absorption property of open-cell metallic foams manufactured by a template replication technique, *Mater. Des.*, 2018, **137**, 108–116, DOI: 10.1016/j.matdes.2017.10.016.

65 L. Chen, H. Ji, Y. Tang, H. Wang and J. Qiu, Enhancing sound absorption of Helmholtz resonators through microlattice metamaterials lining, *Thin-Walled Struct.*, 2025, **215**, 113465, DOI: 10.1016/j.tws.2025.113465.

66 X. Wang, X. Xiao, J. Han and Y. He, Honeycomb-cored hierarchical acoustic metamaterials: A synergistically coupled architecture for enhanced broadband sound absorption, *Compos. Struct.*, 2025, **370**, 119409, DOI: 10.1016/j.compstruct.2025.119409.

67 G. d. N. Almeida, E. F. Vergara, L. R. Barbosa, A. Lenzi and O. M. Silva, On the use of metamaterials with negative effective parameters for dual sound energy control, *Appl. Acoust.*, 2024, **221**, 110010, DOI: 10.1016/j.apacoust.2024.110010.

68 D. Ramos, F. Pompoli, C. Marescotti, L. Godinho, P. Amado-Mendes and P. Mareze, Modelling the effective sound propagation properties of a hexagonal acoustic metamaterial using a dissipative equivalent-fluid approach under different termination conditions, *J. Sound Vib.*, 2025, **598**, 118855, DOI: 10.1016/j.jsv.2024.118855.

69 W. Yu, J. Ren, Y. Zhang, D. Wang, M. Zhang, B. Song, C. Shen and A. Zhao, High-temperature acoustic absorption for circular-ring slit type perforated porous metamaterial, *Eng. Struct.*, 2025, **338**, 120612, DOI: 10.1016/j.engstruct.2025.120612.

70 Y. Fei, W. Fang, M. Zhong, J. Jin, P. Fan, J. Yang, Z. Fei, L. Xu and F. Chen, Extrusion Foaming of Lightweight Polystyrene Composite Foams with Controllable Cellular Structure for Sound Absorption Application, *Polymers*, 2019, **11**(1), 106, DOI: 10.3390/polym11010106.

71 M. Sabbagh and A. Elkhateeb, Sound Absorption Characteristics of Polyurethane and Polystyrene Foams as Inexpensive Acoustic Treatments, *Acoust. Aust.*, 2019, **47**, 285–304, DOI: 10.1007/s40857-019-00168-z.

72 Z. Liu, J. Zhan, M. Fard and J. L. Davy, Acoustic properties of a porous polycarbonate material produced by additive manufacturing, *Mater. Lett.*, 2016, **181**, 296–299, DOI: 10.1016/j.matlet.2016.06.045.

73 K. Kalauni and S. J. Pawar, A review on the taxonomy, factors associated with sound absorption and theoretical modeling of porous sound absorbing materials, *J. Porous Mater.*, 2019, **26**, 1795–1819, DOI: 10.1007/s10934-019-00774-2.

74 H. S. Seddeq, N. M. Aly, A. Marwa A and M. H. Elshakankery, Investigation on sound absorption properties for recycled fibrous materials, *J. Ind. Text.*, 2013, **43**, 56–73, DOI: 10.1177/1528083712446956.